#### **OPEN ACCESS**



# Photometric Survey of Neptune's Trojan Asteroids. I. The Color Distribution

#### **Abstract**

In 2018, Jewitt identified the "The Trojan Color Conundrum," namely that Neptune's Trojan asteroids (NTs) had no ultrared members, unlike the the nearby Kuiper Belt. Since then, numerous ultrared NTs have been discovered, seemingly resolving this conundrum. However, it is still unclear whether or not the Kuiper Belt has a color distribution consistent with the NT population, as would be expected if it were the source population. In this work, we present a new photometric survey of 15 out of 31 NTs. We utilized the Sloan g'r'i'z' filters on the IMACS f/4 instrument, which is mounted on the 6.5 m Baade telescope. In this survey, we identify four NTs as being ultrared using a principal component analysis. This result brings the ratio of red to ultrared NTs to 7.75:1, more consistent with the corresponding trans-Neptunian object ratio of 4–11:1. We also identify three targets as being blue (nearly solar) in color. Such objects may be C-type surfaces, but we see more of these blue NTs than has been observed in the Kuiper Belt. Finally, we show that there are hints of a color-absolute magnitude (H) correlation, with larger H (smaller sized, lower albedo) tending to be more red, but more data are needed to confirm this result. The origin of such a correlation remains an open question that will be addressed by future observations of the surface composition of these targets and their rotational properties.

*Unified Astronomy Thesaurus concepts:* Trojan asteroids (1715); Neptune trojans (1097); Multi-color photometry (1077); CCD photometry (208)

#### 1. Introduction

Trojan asteroids are planetary companions that reside in the asymmetric 1:1 mean motion resonance of planets; these asteroids librate at the planet—Sun L4 and L5 Lagrange points, meaning that they have the same orbit as the planet but librate about a point 60° ahead of (L4) or behind (L5) the planet. Numerical simulations show that orbits of Trojan asteroids can be quite stable, on order the age of the solar system (Lykawka et al. 2011; Ćuk et al. 2012; Gomes & Nesvorný 2016). Therefore, the stable members of these populations are likely relatively undisturbed remnants of our primordial planetary disk. The physical properties of these populations can thus give us a window into the early solar system.

However, Neptune's Trojan asteroids (NTs) are not thought to have formed in situ. Rather, this population likely grew through capture of planetesimals during the epoch of planetary migration, during which the outer planets migrated from the location of their formation to their present-day locations (Fernandez & Ip 1984; Malhotra 1993, 1995; Hahn & Malhotra 1999). Assuming that Neptune migrated significantly in its early evolution, the Lagrange points must have also migrated with it (Kortenkamp et al. 2004) Therefore, the NT population can be used to constrain migratory models (Nesvorný et al. 2013; Gomes & Nesvorný 2016; Pike et al. 2017b; Nesvorný et al. 2018). Such migration would have occurred in the first several hundred megayears in the history of the solar system, so while these objects may not have formed in situ, they still are remnants of the very early solar system.

Such models show that primordial Jupiter Trojan populations do not survive this planetary migration, indicating that they

Original content from this work may be used under the terms of the Creative Commons Attribution 4.0 licence. Any further distribution of this work must maintain attribution to the author(s) and the title of the work, journal citation and DOI.

must have originated from elsewhere in the solar system (Roig & Nesvorný 2015). Similarly, since the dynamics of planetary migration likely dispersed any primordial NTs as well, from where did the current population of NTs originate? The most likely source is the nearby Kuiper Belt. If that were the case, one would expect these two populations to be similar in size and color (surface composition). Regarding the color of the Kuiper Belt objects (KBOs), the bimodality of red (g - i < 1.2)versus ultrared (g-i > 1.2) members has been well established (Sheppard 2010; Schwarz et al. 2011; Hainaut et al. 2012; Peixinho et al. 2012; Sheppard 2012; Lacerda et al. 2014; Peixinho et al. 2015; Pike et al. 2017a; Wong & Brown 2017; Schwamb et al. 2019). Similarly, the centaur population, small bodies that orbit between Jupiter and Neptune, are thought to be fed by planetesimals escaping the NT region (Horner & Lykawka 2010). These objects are also red/ultrared in color (Peixinho et al. 2012, 2015).

Through 2018, no ultrared NTs had been found, making their color distribution distinctly different from their expected origins or offshoots. Termed the "Trojan color conundrum," this tension is not easy to resolve (Jewitt 2018). One explanation is that some sort of resurfacing has happened to the NT population specifically that affected neither the centaurs nor KBOs. Jupiter's Trojan population is also devoid of ultrared members, which is thought to be due to thermal resurfacing (Luu & Jewitt 1996; Jewitt 2002). However, the temperatures at the distance of Neptune are too cold for such a scenario to be valid (Jewitt 2018). Another potential explanation is collisional resurfacing, which could strip the ultrared crust off of the surfaces of these bodies, revealing a bluer surface underneath. One source of such collisions could be Plutinos, 3:2 resonators with Neptune, which have significant orbital overlap with the NT population (Almeida et al. 2009). Such collisions are expected to occur when Plutinos have high libration amplitudes, high eccentricities, and low inclinations;

Table 1 NT Targets of This Survey

Name	L4/L5	e	i	Н	Date Observed	Ave. r	g-r	r–i	r-z	Color Class.
2006 RJ 1,2	L4	0.03	8.2	7.56	113021	21.97	$0.59 \pm 0.045$	$0.16 \pm 0.035$	$0.17 \pm 0.058$	red
					120222	21.88			$0.24\pm0.055$	indeterminate
2007 VL <sup>1,2</sup> <sub>305</sub>	L4	0.07	28.1	8.51	113021	22.60	$0.60\pm0.054$	$0.25\pm0.038$	$-0.15 \pm 0.109$	red
					120222	22.60			$0.30\pm0.047$	indeterminate
2010 TS $^{3}_{191}$	L4	0.05	6.6	8.07	113021	22.39	$0.61\pm0.029$	$0.30\pm0.029$	$0.64\pm0.078$	red
2011 SO $\frac{3}{277}$	L4	0.01	9.6	7.76	113021	22.43	$0.60\pm0.067$	•••	•••	indeterminate
					120222	22.53		$0.57\pm0.050$	$0.82\pm0.047$	ultrared
$2012 \text{ UD } ^{5}_{185}$	L4	0.04	28.3	7.59	113021	22.32	$0.61\pm0.033$	$0.37\pm0.045$	$0.12\pm0.081$	red
2012 UV 5	L4	0.07	20.8	9.28	113021	23.76	$0.71\pm0.058$	$0.23\pm0.051$	•••	red
2013 RL 5 124	L4	0.03	10.1	8.83	113021	23.37	$0.38\pm0.075$	$0.54\pm0.086$	$0.67\pm0.128$	red
2013 TZ <sup>5</sup> <sub>187</sub>	L4	0.07	13.1	8.19	113021	23.27	$0.90\pm0.053$	$0.30\pm0.057$		ultrared
2013 VX 4,5	L4	0.09	31.2	8.31	113021	22.60	$1.01\pm0.043$	$0.44\pm0.043$	$0.86\pm0.049$	ultrared
					091122	22.96	$0.70 \pm 0.104$	$0.47 \pm 0.048$	$0.73 \pm 0.045$	ultrared
2014 RO <sup>5</sup> <sub>74</sub>	L4	0.05	29.5	8.39	120222	23.34	$0.65\pm0.052$	$0.42\pm0.064$	$1.42\pm0.069$	ultrared
2014 SC <sup>5</sup> <sub>374</sub>	L4	0.10	33.7	8.18	113021	23.24	$0.43\pm0.066$	$0.12\pm0.081$		blue
2014 YB 925	L4	0.10	30.8	8.62	091222	23.41	$0.46 \pm 0.187$	$0.07 \pm 0.100$	$0.36 \pm 0.090$	blue
2015 VU 5 207	L4	0.03	38.9	7.28	080922	22.23	$0.31\pm0.034$	$0.24\pm0.031$	$0.40\pm0.024$	red
					091122	22.10	$0.47\pm0.052$	$0.09 \pm 0.068$	$0.35\pm0.028$	blue
2015 VV <sup>5</sup> <sub>165</sub>	L4	0.09	16.8	9.02	113021	23.32	$0.87\pm0.049$	$0.32\pm0.055$	<del></del>	ultrared
$2015 \text{ VW}_{165}^5$	L4	0.05	5.0	8.39	113021	22.89	$0.45\pm0.032$	$0.36\pm0.048$	•••	red
					120222	22.93	•••		$0.61\pm0.060$	indeterminate

Note. Column (1): object designation; has previous color measurements taken from (1) Sheppard (2012), (2) Parker et al. (2013), (3) Jewitt (2018), (4) Lin et al. (2019), and (5) Bolin et al. (2023). Column (2): Lagrange point. Column (3): eccentricity. Column (4): inclination (deg). Column (5): absolute magnitude. Column (6): dates observed. Column (7): measured average SDSS r-band magnitude. Column (8): measured SDSS g - r (mag). Column (9): measured SDSS r - i (mag). Column (10): measured SDSS r - z (mag). Column (11): color classification determined based on the PCA (see Section 4.2).

therefore, we would expect the color distribution of NTs to be inclination dependent as well, where high-inclination NTs avoid these collisions and retain their ultrared surfaces. Finally, this discrepancy could be due to a primordial boundary between red/ultrared bodies that was subsequently mixed by Neptune's migration (DeMeo & Carry 2014; Neveu & Vernazza 2019). Based on the exact nature of the epochs of radial mixing, mass removal, and planet migration, the resulting NT population could be devoid of ultrared members while the Centaur population is not (Neveu & Vernazza 2019), but specific simulations of these two populations have not been conducted. This hypothesis has been supported by the discovery of two trans-Neptunian object (TNO)—like (red) objects all the way in the asteroid belt (Hasegawa et al. 2021).

In 2019, the first ultrared NT, 2013VX<sub>30</sub>, was discovered (Lin et al. 2019), and additional ultrared NTs have been discovered since then (Bolin et al. 2023). On the surface, these discoveries seem to resolve the conundrum. However, the color distribution of NTs still appears distinct from that of other TNO populations (Bolin et al. 2023). Further observations of the NT population are needed to determine whether or not these distributions are truly distinct.

The structure of this paper is as follows: Section 2 describes the design of our photometric survey. Section 3 outlines our data reduction process. Section 4 presents the results of our survey. Section 5 discusses the meaning of our results. Section 6 provides conclusions drawn from these results.

# 2. Survey Design

The goal of this paper is to measure the optical colors of currently known NTs in order to better understand the physical characteristics of their surfaces. The targets are listed in Table 1. All of our targets have been previously observed but not by the same survey. All of our targets, except  $2015VU_{207}$ , were already known to be stable for  $\sim \! 1$  Gyr (Lin et al. 2021, 2022). Following the methods of Lin et al. (2022), we find that  $2015VU_{207}$  is also stable for 1 Gyr in our simulations.

We used the IMACS f/4 instrument on the 6.5m Baade telescope at Las Campanas Observatory on four unique nights to observe this population. IMACS was most suitable for this task with its optical wavelength coverage ( $\sim$ 400–900 nm) and large field of view to account for the positional uncertainty of the targets. The Sloan g'r'i'z' filters were used for our photometric measurements. In order to account for any variation due to a target's rotational period, we observed each target with "bounding" r'-band observations (i.e., each observation in a different filter was preceded and followed by an observation in r'). We chose r' to be the bounding observations since this filter reaches the highest signal-to-noise ratio in the shortest amount of time. The fast readout mode with  $2 \times 2$  binning was used.

#### 3. Photometric Reduction

#### 3.1. Calibration

To calibrate the photometry of our IMACS observations, we cross-matched the in-frame background stars against PS1 sources (Magnier et al. 2013). We first converted the PS1 griz photometry to the Sloan Digital Sky Survey (SDSS) system using the transformation equations in Tonry et al. (2012), and then we selected the sources with g-r between 0.25 and 2.0 and r-i between 0.0 and 0.8 as the reference sources. By solving the equation below using the apparent magnitude of the reference sources, we determined the photometric zero-point of

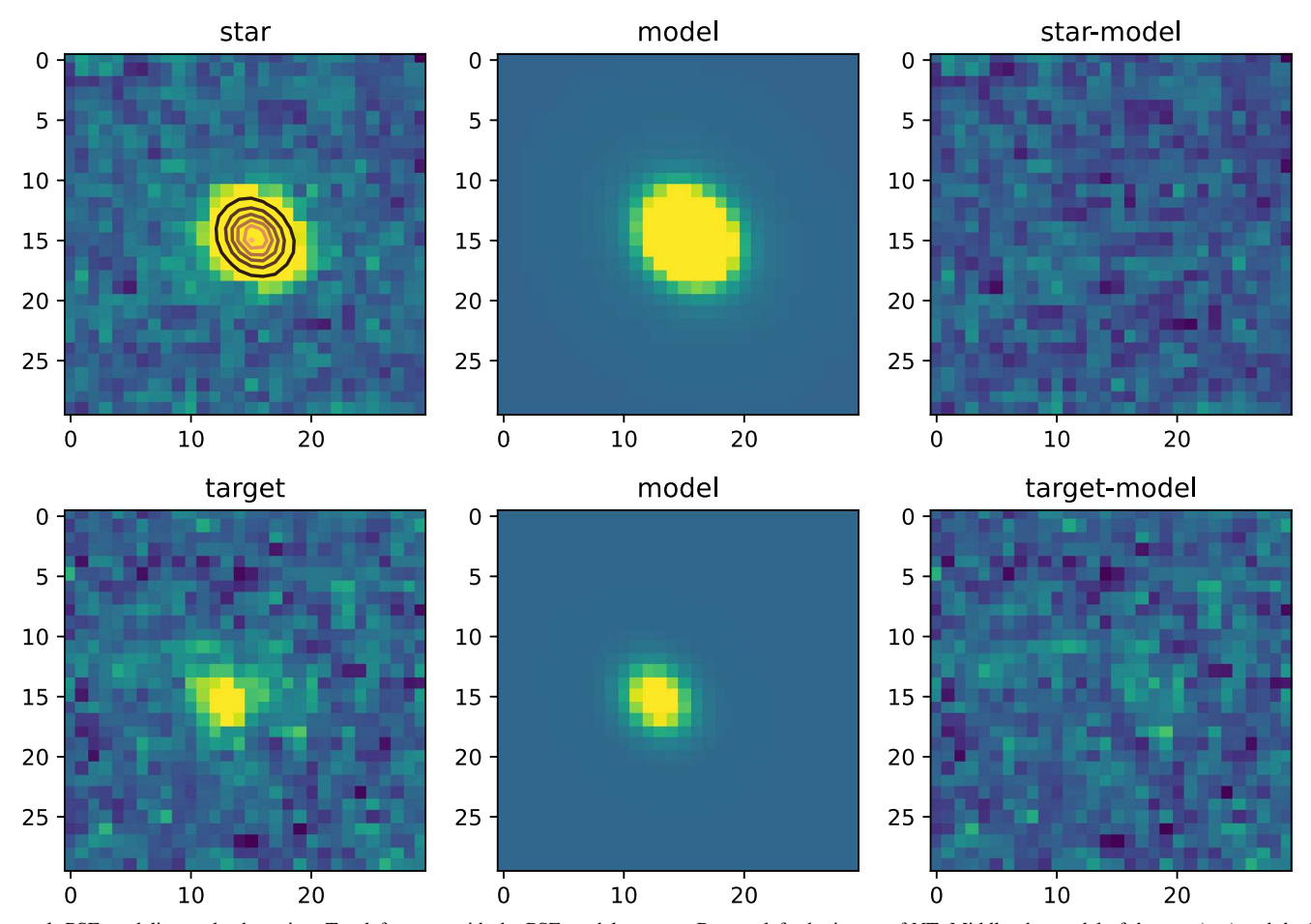


Figure 1. PSF modeling and subtraction. Top left: a star with the PSF model contour. Bottom left: the image of NT. Middle: the model of the star (top) and the NT (bottom). Right: the images after subtraction of the model.

each frame:

$$m_{\text{sdss}} = m_{\text{ins}} + 2.5 \log_{10}(\tau_{\text{exp}}) + m_0,$$
 (1)

where  $m_{\rm sdss}$  is the apparent magnitude of a specific band of the cross-matched reference sources,  $m_{\rm ins}$  is the instrumental magnitude of that specific band measured from the IMACS image,  $\tau_{\rm exp}$  is the exposure time, and  $m_0$  is the photometric zero-point of that frame.

After we determined the zero-points of each frame, we used every cross-matched star in every frame to evaluate the linear color conversions between the IMACS and SDSS photometric systems by solving the following equation:

$$m_M = m_{\rm sdss} + a (g - r)_{\rm sdss} + b, \qquad (2)$$

where  $m_M$  and  $m_{\rm sdss}$  are the IMACS and SDSS magnitude, respectively, and a, b are the coefficients of the linear conversion. The results are

$$g_{M} = g_{\text{sdss}} - 0.078(g - r)_{\text{sdss}} + 0.069$$

$$r_{M} = r_{\text{sdss}} - 0.024(g - r)_{\text{sdss}} + 0.024$$

$$r_{M} = r_{\text{sdss}} - 0.038(r - i)_{\text{sdss}} + 0.015$$

$$i_{M} = i_{\text{sdss}} - 0.188(r - i)_{\text{sdss}} + 0.134$$

$$z_{M} = z_{\text{sdss}} - 0.026(g - r)_{\text{sdss}} + 0.031.$$
(3)

With the photometric zero-points and the color conversion equations, we are able to measure the griz colors of targets in the SDSS photometry system.

# 3.2. PSF Modeling

To accurately measure the flux and apparent magnitude of NTs, we select stars around the target NT to model the local point-spread function (PSF). Several popular analytical functions are considered for modeling the PSF, such as Moffat (Moffat 1969) and the sum of 2D Gaussians (Bendinelli et al. 1990). Both functions can adequately model the "wing" of the PSF. However, considering that our PSF can be asymmetric (not round; see Figure 1), we model the PSF by using the superposition of n asymmetric 2D Gaussians. The flux of the PSF at any point in the (x', y') orthogonal coordinate system is

$$PSF(x', y') = b(x', y') + \sum_{i=1}^{n} A_{i}$$

$$\times \left( exp \left[ -\left(\frac{x'^{2}}{2\sigma_{x'i}^{2}} + \frac{y'^{2}}{2\sigma_{y'i}^{2}}\right) \right] \right), \tag{4}$$

where b(x', y') is the background flux at that point, n is a small number,  $A_i$  is the amplitude of individual Gaussians, and  $\sigma_{x'i}$  and  $\sigma_{y'i}$  are the widths on x'- and y'-axes of individual Gaussians, respectively. This equation can be rotated to the image reference frame (x, y) with a position angle  $\theta$  and translating the centroid to  $(x_0, y_0)$  such that

$$\begin{pmatrix} x' \\ y' \end{pmatrix} = \begin{bmatrix} \cos \theta & -\sin \theta \\ \sin \theta & \cos \theta \end{bmatrix} \begin{pmatrix} x - x_0 \\ y - y_0 \end{pmatrix}.$$

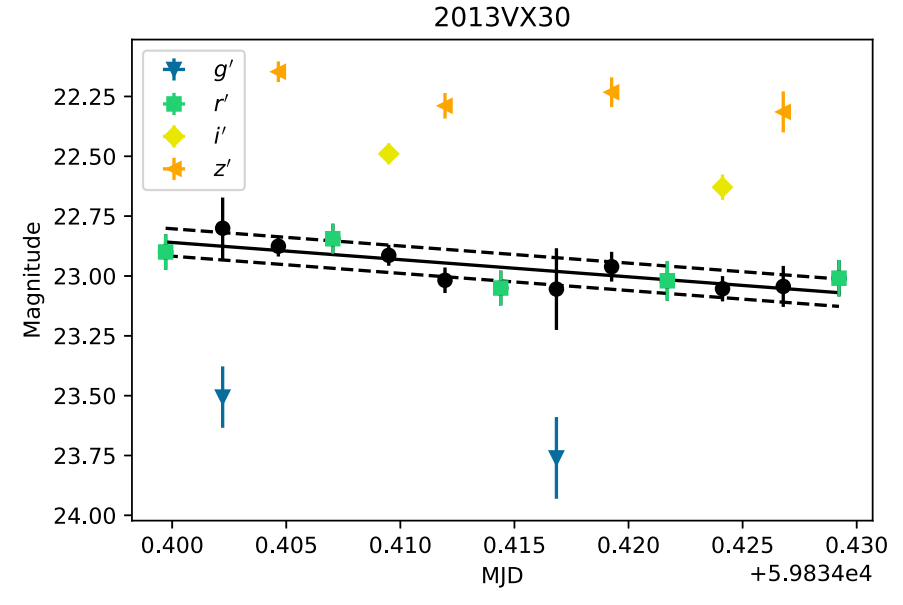


**Figure 2.** This figure shows our least-squares approach to fitting r'-band light curves and colors for an example NT target, 2013 VX30. Each observation is shown as a colored point (blue downward-pointing triangle for g', green square for r', yellow diamond for i', and orange leftward-pointing triangle for g'. We then used a constant but free-parameter color term to convert each observation to an r'-band observation; these points are shown as black circles. The solid line is our least-squares fit to the r'-band (black) points. The dotted lines show our  $1\sigma$  deviation from this fit.

Therefore, the Gaussian functions share the same center, position angle, and ellipticity but have unequal contribution and different width. To properly choose "n," the number of Gaussians we should use, we calculate the Bayesian information criterion (BIC) for each n we use. The BIC is defined as

$$BIC = -2 \ln(\hat{\mathcal{L}}) + k \ln(m), \tag{5}$$

where  $\hat{\mathcal{L}}$  is the maximum likelihood of the model, k is the number of parameters estimated by the model, and m is the number of data points we use to fit the model. The models with lower BIC values are generally preferred, which penalizes the model with larger k automatically. Since the multiple Gaussian PSF model can be linearized by taking the logarithm and assuming that the errors are normally distributed, the  $\hat{\mathcal{L}}$  is equivalent to the least-squares estimation. Thus, BIC can be written as a function of error variance  $\hat{\sigma}_e^2$ :

$$BIC = m \ln(\hat{\sigma_e^2}) + k \ln(m). \tag{6}$$

In other words, the model with lower residual and fewer parameters is preferred. We find that the model with n=1, a single 2D Gaussian, always has the highest BIC. On the other hand, the models with n=2 and n=3 generally have similar BICs; therefore, we conclude that using any model with n>3 is redundant.

Finally, we use the PSF model with n = 2 or 3, depending on which one has a lower BIC. Once all of the parameters are measured via modeling the stars, the target NT can be modeled by refitting the center and amplitude of the PSF. The flux is the sum of the final model. Figure 1 demonstrates that both the star and the NT can be properly subtracted by the PSF model.

# 3.3. Rotation Curve Correction

The observed magnitudes and the resulting colors we are trying to measure are subject to rotational variations on the surface of these objects. To approximately account for this, we use a model that exhibits a linear variation in source brightness (its r'-band magnitudes) and constant g' - r', r' - i', r' - z' colors (to convert each measurement to an r'-band magnitude). This model was then fit using a least-squares approach (see Figure 2). The resulting colors have been converted to SDSS magnitudes (griz; see Equation (3)), which are reported in Table 1.

### 3.4. Reddening Line

Taken from Hainaut & Delsanti (2002), the reddening, or the spectral index, can be expressed as the percent of reddening per 100 nm:

$$S(\lambda_{\rm l}, \lambda_{\rm 2}) = 100* \frac{R(\lambda_{\rm 2}) - R(\lambda_{\rm l})}{(\lambda_{\rm 2} - \lambda_{\rm l})/100},$$
 (7)

where  $R(\lambda)$  is taken from Jewitt & Meech (1986),

$$R(\lambda) = 10^{-0.4(m(\lambda) - m_{\odot}(\lambda))},\tag{8}$$

such that  $m(\lambda)$  and  $m_{\odot}(\lambda)$  are the magnitudes of the object and the Sun, respectively, at a particular wavelength,  $\lambda$ . Setting the reddening line to pass through the color of the Sun (i.e., for  $S(\lambda_1, \lambda_2) = 0$ ,  $m(\lambda_1) - m(\lambda_2) = m_{\odot}(\lambda_1) - m_{\odot}(\lambda_2)$ ), we can derive the following equation, assuming  $m(\lambda_1) = m_{\odot}(\lambda_1)$ :

$$m(\lambda_2) = -2.5 \log[1 - 10^{-4} S(\lambda_1, \lambda_2)(\lambda_1 - \lambda_2)] + m_{\odot}(\lambda_2).$$
(9)

Assuming that  $S(\lambda_1, \lambda_2)$  varies from -10% to 80%, we can plot the reddening line for g-r versus r-i and g-r versus r-z in Figures 3 and 4, respectively. Note that our targets generally fall along the reddening line, as has been observed for small bodies in the outer solar system previously (Hainaut & Delsanti 2002). Objects that fall above/below the reddening line must exhibit emission/absorption lines at those particular wavelengths, causing them to deviate from a flat spectral index.

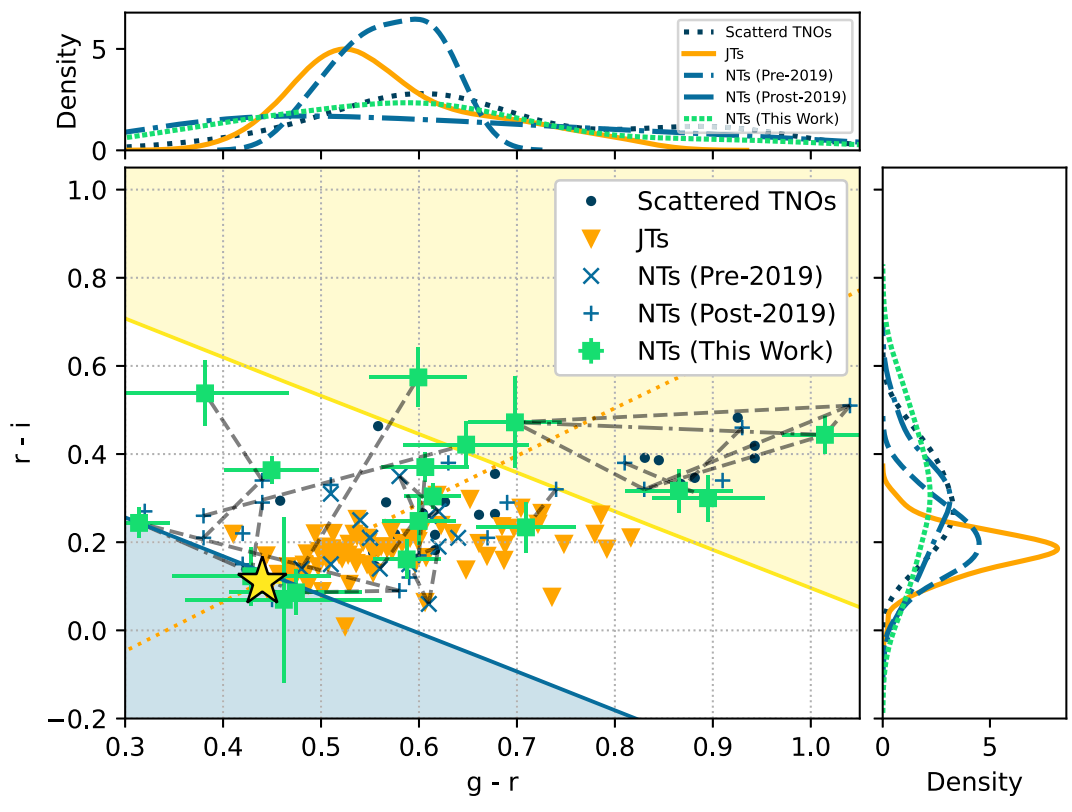


Figure 3. Measured g - r vs. r - i of the NT population. Blue points are colors of scattered TNOs, and orange triangles are JTs, both taken from the literature (Hainaut et al. 2012). Light-blue crosses are previously observed colors of NTs that the "Trojan color conundrum" was based on (Sheppard & Trujillo 2006; Sheppard 2012; Parker et al. 2013; Jewitt 2018), while the blue plus signs are more recently observed NT colors that bring this conundrum into question (Lin et al. 2019; Bolin et al. 2023). Targets observed in this paper are shown as green squares. Solar color and the reddening line (see Section 3.4) are depicted as a yellow star and orange dotted line, respectively. Objects that have multiple observed in this paper are connected by a dotted—dashed line. NTs that have been previously observed in the literature are connected by a dashed line. The yellow line marks values where the PCA yields values equal to our cutoff of 1.75 (see Figure 6 and Section 4.2). Objects in the yellow region are above this cutoff and considered ultrared in this paper. The blue line marks values where the PCA yields values equal to our cutoff of -1.25 (see Figure 6 and Section 4.2). Objects in the blue region are bluer than this cutoff and considered blue in this paper. The top and right inset plots show the kernel density estimation (KDE) of the g - r and r - i distributions, respectively, of the included subpopulations.

#### 4. Results

#### 4.1. Color-Color Results

In Figure 3, we show the g-r and r-i colors measured for our NT targets. Similar to the scattered TNOs, our targets exhibit wide range in this color space; while most targets fall within the "red" zone (principal component <1.75; see Section 4.2), there are three firm NTs and one potential NT in the "ultrared" zone (principal component >1.75). Of these objects, we identified two new ultrared NTs, 2013 TZ<sub>187</sub> and 2015 VV<sub>165</sub>, which were also independently found and reported in Bolin et al. (2023). The potential "ultrared" NT, 2011 SO<sub>277</sub>, has varying results from different observations (Jewitt 2018; Lin et al. 2019; this work); see more discussion of this object in Section 4.4.

With extra ultrared colored NTs, the red-to-ultrared ratio for our sample is 3.75:1, or 7.75:1 for the entire known population. This ratio is much more consistent with the dynamically excited KBO ratio of between 4:1 and 11:1 (Schwamb et al. 2019). However, comparing these ratios is not sufficient to determine whether the NT and KBO populations come from the same source distribution (see Section 4.2). We also show the KDEs of g - r and r - i color in Figure 3. Unlike the results from previous works, which claimed that the NTs and JTs have very similar color distributions, our new results show that the

KDEs of NTs are closer to the KDEs of scattered TNOs. Further analysis is presented in Section 4.2.

In Figure 4, we show the g-r and r-z colors measured for our NT targets. All of our targets are consistent with the scattered/hot TNO populations. This result is expected, as NTs are thought to have originated from scattered/unstable TNOs. The physical cause of this z-band colorization of the cold TNO population is not currently clear but must be due to some absorption feature around 900 nm based on the displacement from the reddening line. Spectroscopic information, such as will be taken with JWST (Markwardt et al. 2021), will shed further light on chemical links between these populations.

# 4.2. Comparison to Previous Observations

All of the targets in our sample have previous observations (though not all from the same survey). Therefore, we compare the difference between our measurements and those from the literature to our computed errors, shown in Figure 5, to determine whether there is any systematic offset in our observations. We find that the observed differences in g-r are mostly within our observational errors, meaning that our observations are roughly consistent with previous literature. However, previous observations are split between being slightly systematically larger in r-i and being systematically lower than our measurements. Further investigation indicated that the larger group has smaller offset on the order of 0.05, and

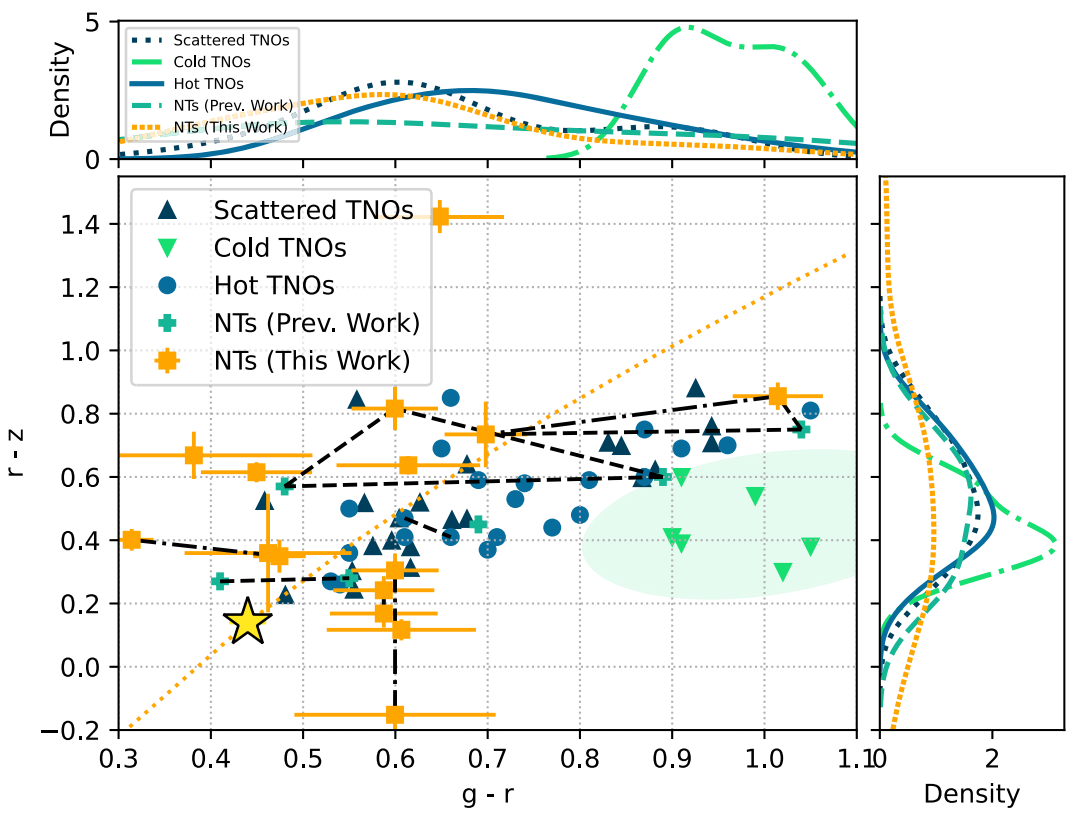
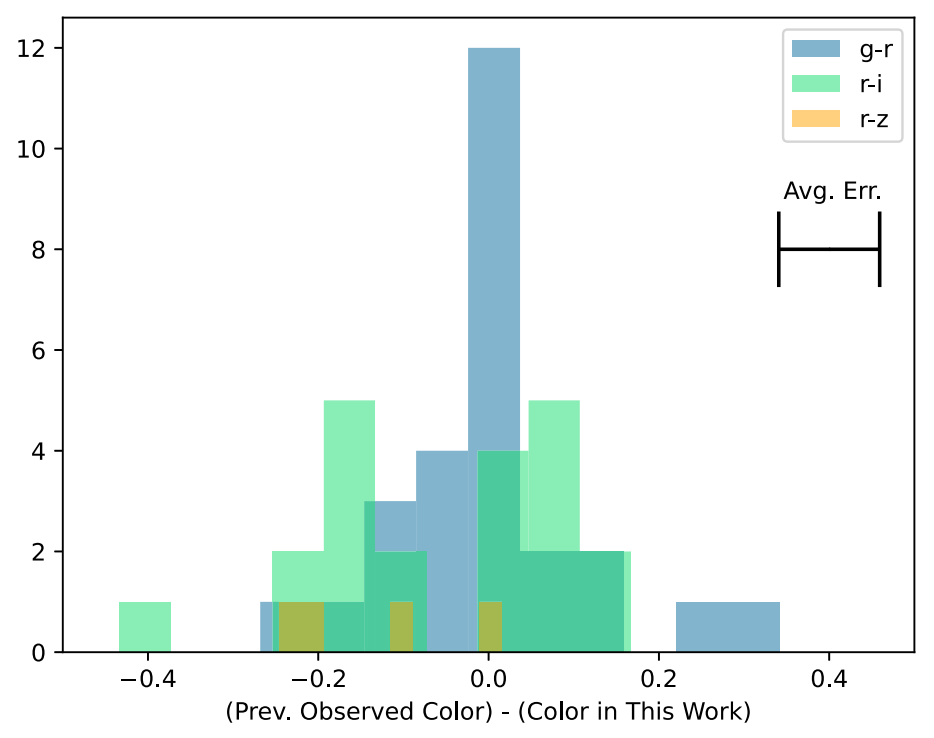
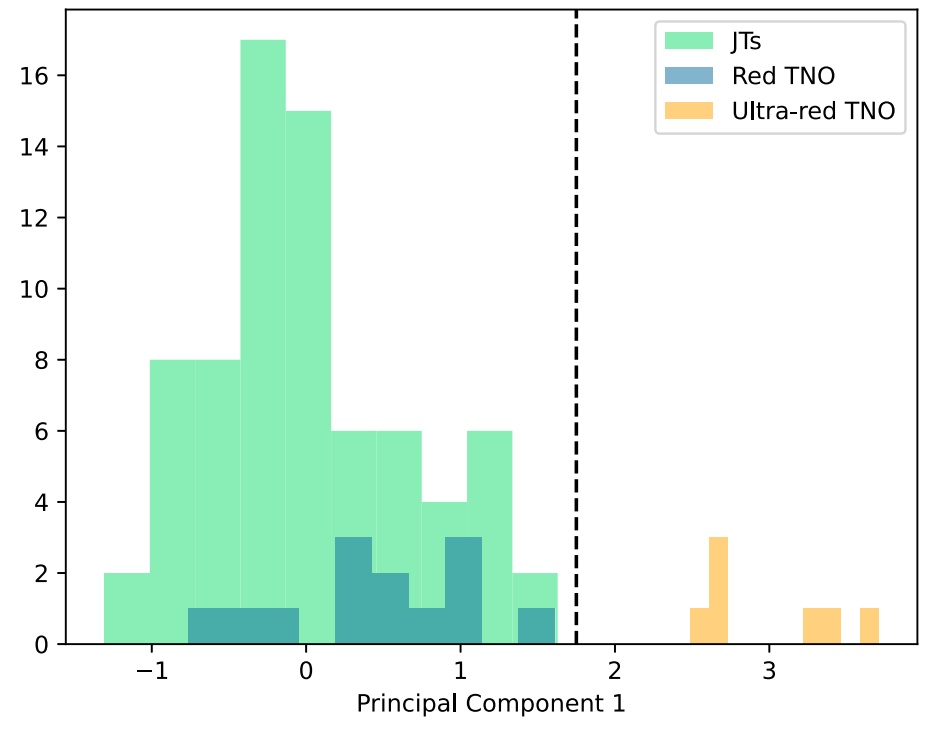


Figure 4. Measured g - r vs. r - z of the NT population. Navy upward-pointing triangles, green downward-pointing triangles, and blue circles are measurements taken from the literature of TNOs (scattered, cold, and hot, respectively; Schwamb et al. 2019). Teal plus signs are colors of NTs taken from the literature (Lin et al. 2019). Targets observed in this paper are shown as orange squares. Solar color and the reddening line (see Section 3.4) are depicted as a yellow star and orange dotted line, respectively. Objects that have observations taken in this paper and from the literature are connected with a dashed line. Objects that have multiple observations in this paper are connected by a dotted-dashed line. The green ellipse demarcates the region of color-color space occupied only by cold TNOs. The top and right inset plots show the KDE of the g - r and r - z distributions, respectively, of the included subpopulations.



**Figure 5.** The differences in observed color between NTs in this paper and the literature as compared to the average error on our observations. The differences in g-r, r-i, and r-z observations are shown as blue, orange, and green histograms, respectively. The average g-r, r-i, and r-z errors are shown as blue dotted, green dotted—dashed, and orange dashed lines, respectively.



**Figure 6.** The results of running a PCA with the g-r and r-i colors of certain solar system populations. The green histogram corresponds to the JTs (taken from Hainaut et al. 2012). The blue and orange histograms correspond to the red and ultrared subpopulations of the scattered TNOs, taken from Hainaut et al. (2012); the classification of red vs. ultrared was determined by using a clustering algorithm (DBSCAN; Pedregosa et al. 2011) that separated the TNOs into two subpopulations.

the lower group has larger offset of about -0.15. We also find an instrument dependency on the groups; the smaller offset samples were mostly measured with Gemini and Dark Energy Survey, which both have proper photometry transformation equations to the SDSS system. On the other hand, the larger offset samples were mostly measured by using the R and I filters or without proper photometry transformation equations. Therefore, it is likely that the different photometry systems mostly contribute such systematic offsets. In every case, this did not change the result much on the following principal component analysis (PCA), since the g-r axis is the dominant element on our principal component.

#### 4.3. Comparison to Other Populations

The ultimate goal of this work is to determine how similar the NT colors are to other populations in the solar system. A simple statistical test to measure the likelihood that two distributions are drawn from the same underlying distribution is the Kolmogorov-Smirnov (K-S) test (Darling 1957). Although the K-S test can be generalized to more than a single dimension, the interpretation becomes complicated. For simplicity, we reduce the dimension of our data and use the traditional statistical test. Specifically, we performed a PCA of our data, using the scikit-learn Python package (Pedregosa et al. 2011). Figure 6 demonstrates that the PCA is able to successfully reduce the g-r versus r-i color-color plot to a 1D parameter that still distinguishes between the red and ultrared populations of TNOs and the whole JT population (which is composed of only red objects). The principal component value (PC1) that separates these populations is 1.75 (shown as a dotted line in Figure 6). We use this definition to classify our NT targets as red or ultrared; the corresponding region in g-r versus r-i space is shown in Figure 3 as a

yellow shaded region. We then applied this PCA model to other populations in the solar system, including JTs and previous observations of NTs, the results of which are shown in Figure 7. By eye, the JT population is clearly unique in that it is nearly devoid of any ultrared members (i.e., targets with a PC1 > 1.75). Also of note is that about 25% of the NT targets presented in this paper occupy a unique region of PC1  $\sim -1$ . This region corresponds to blue objects that are not frequently present in the outer solar system populations (see Section 4.4 for a more in-depth discussion of these objects).

We then ran a K-S test for each combination of these solar system populations to determine the likelihood that they came from the same underlying distribution; the results of these tests are recorded in Table 2. We conclude that the compared populations are from different distributions if they have a pvalue of ≤ 0.05, corresponding to a 95% confidence level to reject the null hypothesis. Therefore, we find that the population observed in this work is not consistent with being drawn from the same distribution as the JTs, but is instead more consistent with the TNO population. This result is the opposite of what was found pre-2019, where the NTs were more consistent with the JT population. The results from post-2019 data also show that the NT population is more consistent with the TNO population, but this work shores up this result significantly. Further observations of members of the NT population in particular could also increase the statistical significance of this result. However, we feel confident in claiming that our results show that NTs and TNOs are consistent with coming from the same underlying distribution based on their optical colors with the greatest confidence to date.

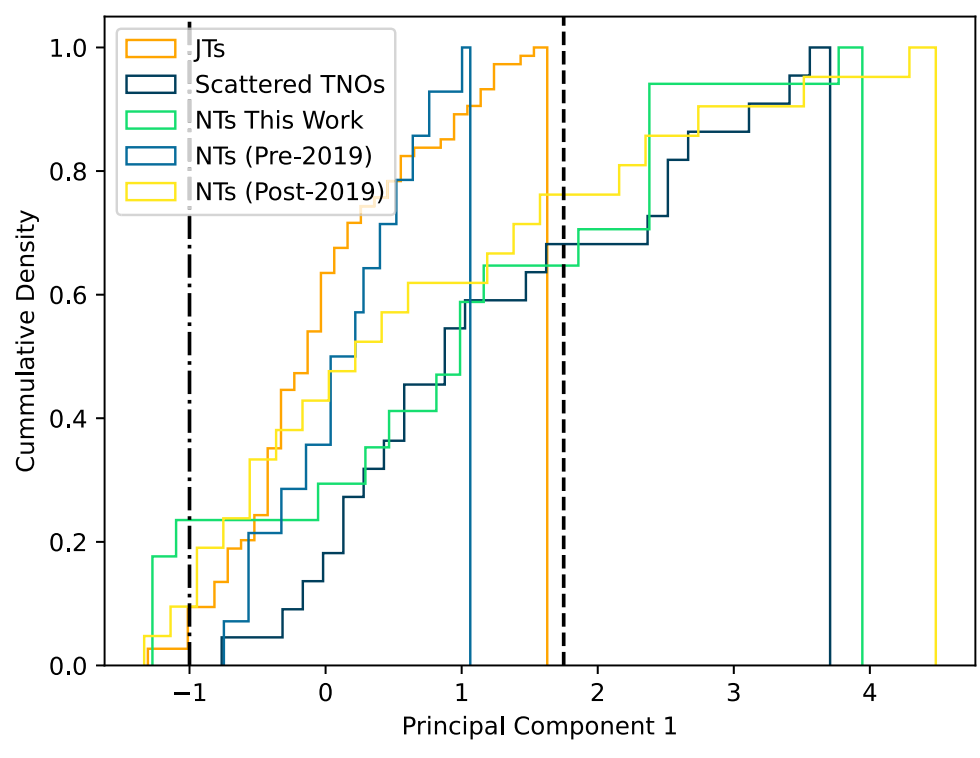


**Figure 7.** Cumulative distributions of the principal component (see Section 4.2) values of populations in the solar system. The cutoff between red and ultrared as defined by this PCA is shown as a black dashed line (see Figure 6). The cutoff between red and blue objects is similarly shown as a dotted–dashed line. The JT and scattered TNO results are shown as orange and navy histograms, respectively. The NT observations from previous literature are shown as a blue histogram. The NT observations from this work are shown as a green histogram.

 Table 2

 The Resulting p-values of the K-S Test on Each Combination of Subpopulations Considered in This Work

	= =				
K-S Test P-value	NTs (This Work)	NTs (Pre-2019)	NTs (Post-2019)	TNOs	JTs
NTs (this work)	1	0.020	0.61	0.56	0.003
NTs (pre-2019)	0.020	1	0.15	0.03	0.27
NTs (post-2019)	0.61	0.15	1	0.14	0.05
TNOs	0.56	0.03	0.14	1	0.000 2
JTs	0.003	0.27	0.05	0.000 2	1

# 4.4. Color-Absolute Magnitude Relations

In Figure 8, we plot the principal component for our targets as a function of absolute magnitude (H). We look for any significant clustering or correlations in these plots that would indicate that the color classification of NTs is dependent on their size.

To search for clustering in our data sets, we run a mean shift clustering algorithm (Pedregosa et al. 2011), which does not need a number of clusters as an input parameter (just a bandwidth that can be initialized with the <code>estimate\_bandwidth</code> function). To test the significance of clustering, we calculate the cluster index. The cluster index from the SigClust evaluation tool is defined as (Ferland et al. 2013)

$$CI = \frac{\sum_{k=1}^{N} \sum_{i \in C_k} ||x_i - \overline{x}^{(k)}||^2}{\sum_{i=1}^{n} ||x_i - \overline{x}||^2},$$
(10)

where  $\bar{x}^{(k)}$  represents the mean of the kth cluster for k = 1, 2, ... N for N clusters and  $\bar{x}$  represents the overall mean. The CI provides a p-value for the significance of the cluster between these two clusters. To test whether our data were correlated, we used the Pearson correlation coefficient (Kirch 2008), which is

defined as

$$r = \frac{\sum (x_i - \bar{x})(y_i - \bar{y})}{\sqrt{\sum (x_i - \bar{x})^2 \sum (y_i - \bar{y})^2}},$$
(11)

where  $x_i$  and  $y_i$  are the data points and  $\bar{x}$  and  $\bar{y}$  are the respective means. We calculated each of these values for all of the plots shown in Figure 8. To determine whether or not these values could be obtained from random noise, we generated 1000 sets of points with the same number of objects as our observation within the same region of principal component versus H space and ran the same analysis on those sets. These results are shown in the inset histograms in Figure 8.

We found that the cluster is consistent with random noise and should not be considered significant. This result also suggests that the colors of NTs are distributed continuously from blue to ultrared rather than bimodally. The positive correlation with size is intriguing and may point to primordial differences in objects of different sizes in the outer solar system. However, H is not a direct correlation to size, as the object's albedo must be taken into account. Such observations do not currently exist for the NT population and will be necessary to establish a color–size correlation. Indeed,

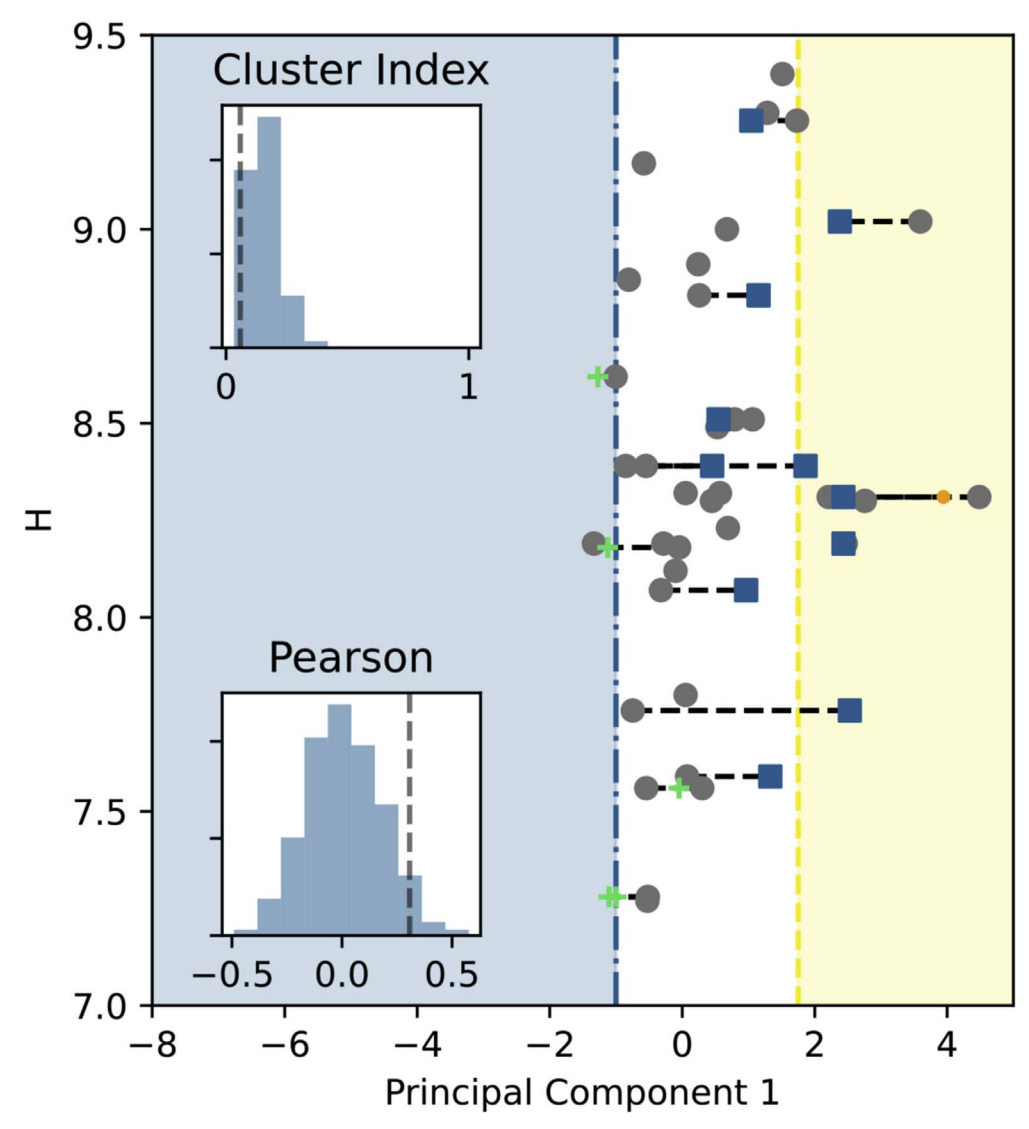


**Figure 8.** NT colors as a function of absolute magnitude. Gray points are taken from the literature (Sheppard & Trujillo 2006; Sheppard 2012; Parker et al. 2013; Jewitt 2018; Lin et al. 2019; Schwamb et al. 2019). Colored squares were measured in this paper. Duplicate observations of the same object are connected by dashed lines. The inset plots contain histograms of the cluster indices and Pearson correlation coefficients of a random distribution of colors and absolute magnitude (see Section 4.1). Each gray dashed line in the inset plots shows the corresponding value calculated for the observed distribution.

photometric observations of the rest of the NT population are necessary to confirm this slight correlation.

# 4.5. Unique Targets

While most of our targets are consistent with previous color measurements, one object,  $2011\,SO_{277}$ , is classified here as ultrared, while its previous observations place it firmly within the red zone. Based on our other observations, we consider our results to be roughly consistent with previous literature (see Figure 5), so this result is indeed unexpected. One explanation as to why this object has such different colors in independent observations is that its surface is not homogeneous. To test this hypothesis, a more in-depth study of the rotational properties of the surface of this object is necessary, which will be upcoming in our next work on the light curves of NTs.

Three of our targets,  $2014\,SC_{375}$ ,  $2014\,YB_{92}$ , and  $2015\,VU_{207}$ , are much bluer, nearly solar in color, as compared to the other NTs or KBOs. Bolin et al. (2023) also reported that  $2014\,YB_{92}$  and  $2015\,VU_{207}$  have blue, near-solar color. In fact, these objects are as blue as the blue B/C-type asteroids, such as

3200 Phaetheon (Tabeshian et al. 2019; Lisse & Steckloff 2022). A similarly blue TNO has been observed, which appears to be covered ferric oxides and phyllosilicates (Seccull et al. 2018). This TNO has a highly eccentric and inclined orbit, suggesting that it may have a common origin with C-type asteroids and has since been implanted into trans-Neptunian space. It is possible that these NTs originated elsewhere in the solar system, but their current orbits are stable for >gigayears (see Section 2), implying that they were captured just after Neptune's migration. However, based on these results, the blue ratio for NTs is currently much higher than that of the TNO population. This result may suggest that inner solar system material may be more efficiently transferred to NT orbits that have a smaller perihelion than the Kuiper Belt. Future spectral observations would be necessary to reveal any compositional differences this target may have as compared to the rest of the NT population.

#### 5. Why Were the Ultrared NTs Rare before 2019?

Prior to 2019, the ultrared NTs were very rare; none of the 13 NT samples in Jewitt (2018) are ultrared NTs, which led to the claim of a "Trojan color conundrum." Here we propose two possibilities to explain this inconsistency:

- 1. Small number statistics: small number statistics could generate such a surprising result. If we assume a 7.75:1 apparent red-to-ultrared ratio of NTs, the chance to randomly select 13 objects without picking up any ultrared one is about 18%, which is very likely. If we use a 3.75:1 apparent red-to-ultrared ratio, the chance is now 0.5%. While it is not impossible, we may also consider alternative explanations.
- 2. Selection effect: since bigger objects are easier to detect and obtain color measurements for, the 13 objects in Jewitt (2018) tend to be large; 10 of 13 have  $H \leq 8$ . Moreover, many NTs have been discovered by deeper (Lin et al. 2021) or wider (Lin et al. 2019; Bernardinelli et al. 2020, 2022) surveys since 2018, which included many high-inclination objects. Thus, the Jewitt (2018) sample appears to be biased toward bigger-sized and lower-inclination objects. In fact, 8 of 13 NTs in the Jewitt (2018) sample have orbital inclination  $<10^{\circ}$ ; 9 of the 31 currently known NTs have inclination <10°, meaning that 8 of the 9 total low-inclination NTs were included in the Jewitt (2018) sample. Such objects have very similar red color (see Figure 8). Therefore, the possible color-orbit-size correlation in NT population could at least partially explain why the "Trojan color conundrum" was observed, especially when there were some selection biases in that sample.

# 6. Conclusions

In this paper, we measure the griz colors for 15 of the 24 known NTs. We used the IMACS f/4 instrument on the 6.5m Baade telescope with Sloan g'r'i'z' filters to conduct our photometric survey. We confirm that 2013 VX<sub>30</sub> is ultrared in color, and we identify three NTs as ultrared. This result brings the red-to-ultrared ratio of NTs to 7.75:1, much more consistent with the corresponding TNO ratio and resolving the "Trojan color conundrum." Moreover, the color distribution of NTs is now indistinguishable from the scattered population of TNOs and different from the Jovian Trojans. We also find three targets that have solar color, the origin of which is unclear; the most likely explanation is that these objects originated from the inner solar system. For the entire NT population, we find that color of NTs may correlated to their absolute magnitude, and the objects with larger H tend to have redder color. The explanation behind this correlation remains an open question that is difficult to address with current data. More discoveries of NTs (especially around L5) are clearly needed. The L5 point has historically been difficult to study owing to its overlap with the Galactic plane, but the NT L5 region is moving away from this high stellar density region, making now the perfect time to start studying this population. The true degree of asymmetry between the L4 and L5 clouds will be important to distinguishing different formation scenarios for the NT population. Moreover, our ongoing work to measure the rotational period and specific composition of these small bodies

directly will be vital to understanding the true origin of the NT population.

### Acknowledgments

This paper includes data gathered with the 6.5 m Magellan Telescopes located at Las Campanas Observatory, Chile.

This material is based on work supported by the National Aeronautics and Space Administration under grant No. NNX17AF21G issued through the SSO Planetary Astronomy Program, by the National Science Foundation under grant No. AST-2009096, and the Space Telescope Science Institute under grant No. JWST-GO-02550.004. L.M. was supported by a University of Michigan Rackham Dissertation Fellowship. This research was supported in part through computational resources and services provided by Advanced Research Computing at the University of Michigan, Ann Arbor.

#### **ORCID iDs**

```
Larissa Markwardt  https://orcid.org/0000-0002-2486-1118
Hsing Wen Lin
(林省文) https://orcid.org/0000-0001-7737-6784
David Gerdes https://orcid.org/0000-0001-6942-2736
Fred C. Adams https://orcid.org/0000-0002-8167-1767
```

```
References
Almeida, A. J. C., Peixinho, N., & Correia, A. C. M. 2009, A&A, 508, 1021
Bendinelli, O., Parmeggiani, G., Zavatti, F., & Djorgovski, S. 1990, AJ,
Bernardinelli, P. H., Bernstein, G. M., Sako, M., et al. 2020, ApJS, 247, 32
Bernardinelli, P. H., Bernstein, G. M., Sako, M., et al. 2022, ApJS, 258, 41
Bolin, B. T., Fremling, C., Morbidelli, A., et al. 2023, MNRAS, 521, L29
Ćuk, M., Hamilton, D. P., & Holman, M. J. 2012, MNRAS, 426, 3051
Darling, D. A. 1957, Ann. Math. Stat., 28, 823
DeMeo, F. E., & Carry, B. 2014, Natur, 505, 629
Ferland, G. J., Porter, R. L., van Hoof, P. A. M., et al. 2013, RMxAA, 49, 137
Fernandez, J. A., & Ip, W. H. 1984, Icar, 58, 109
Gomes, R., & Nesvorný, D. 2016, A&A, 592, A146
Hahn, J. M., & Malhotra, R. 1999, AJ, 117, 3041
Hainaut, O. R., Boehnhardt, H., & Protopapa, S. 2012, A&A, 546, A115
Hainaut, O. R., & Delsanti, A. C. 2002, A&A, 389, 641
Hasegawa, S., Marsset, M., DeMeo, F. E., et al. 2021, ApJL, 916, L6
Horner, J., & Lykawka, P. S. 2010, MNRAS, 402, 13
Jewitt, D. 2018, AJ, 155, 56
Jewitt, D., & Meech, K. J. 1986, ApJ, 310, 937
Jewitt, D. C. 2002, AJ, 123, 1039
2008, in Pearson's Correlation Coefficient, Kirch, W. (ed.) (Dordrecht:
   Springer), 1090
Kortenkamp, S. J., Malhotra, R., & Michtchenko, T. 2004, Icar, 167, 347
Lacerda, P., Fornasier, S., Lellouch, E., et al. 2014, ApJL, 793, L2
Lin, H. W., Chen, Y.-T., Volk, K., et al. 2021, Icar, 361, 114391
Lin, H. W., Gerdes, D. W., Hamilton, S. J., et al. 2019, Icar, 321, 426
Lin, H.-W., Markwardt, L., Napier, K. J., Adams, F. C., & Gerdes, D. W. 2022,
   RNAAS, 6, 79
Lisse, C., & Steckloff, J. 2022, Icar, 381, 114995
Luu, J., & Jewitt, D. 1996, AJ, 112, 2310
Lykawka, P. S., Horner, J., Jones, B. W., & Mukai, T. 2011, MNRAS,
   412, 537
Magnier, E. A., Schlafly, E., Finkbeiner, D., et al. 2013, ApJS, 205, 20
Malhotra, R. 1993, Natur, 365, 819
Malhotra, R. 1995, AJ, 110, 420
Markwardt, L., Adams, F., Gerdes, D., et al. 2021, JWST Proposal, 2550
Moffat, A. F. J. 1969, A&A, 3, 455
Nesvorný, D., Vokrouhlický, D., Bottke, W. F., & Levison, H. F. 2018, NatAs,
Nesvorný, D., Vokrouhlický, D., & Morbidelli, A. 2013, ApJ, 768, 45
Neveu, M., & Vernazza, P. 2019, ApJ, 875, 30
Parker, A. H., Buie, M. W., Osip, D. J., et al. 2013, AJ, 145, 96
Pedregosa, F., Varoquaux, G., Gramfort, A., et al. 2011, JMLR, 12, 2825
Peixinho, N., Delsanti, A., & Doressoundiram, A. 2015, A&A, 577, A35
```

Peixinho, N., Delsanti, A., Guilbert-Lepoutre, A., Gafeira, R., & Lacerda, P. 2012, A&A, 546, A86

Pike, R. E., Fraser, W. C., Schwamb, M. E., et al. 2017a, AJ, 154, 101 Pike, R. E., Lawler, S., Brasser, R., et al. 2017b, AJ, 153, 127

Roig, F., & Nesvorný, D. 2015, AJ, 150, 186

Schwamb, M. E., Fraser, W. C., Bannister, M. T., et al. 2019, ApJS, 243, 12

Schwarz, G. J., Ness, J.-U., Osborne, J. P., et al. 2011, ApJS, 197, 31

Seccull, T., Fraser, W. C., Puzia, T. H., Brown, M. E., & Schönebeck, F. 2018, ApJL, 855, L26

Sheppard, S. S. 2010, AJ, 139, 1394 Sheppard, S. S. 2012, AJ, 144, 169

Sheppard, S. S., & Trujillo, C. A. 2006, Sci, 313, 511

Tabeshian, M., Wiegert, P., Ye, Q., et al. 2019, AJ, 158, 30 Tonry, J. L., Stubbs, C. W., Lykke, K. R., et al. 2012, ApJ, 750, 99

Wong, I., & Brown, M. E. 2017, AJ, 153, 145